Mormyroidea-inspired electronic skin for active non-contact three-dimensional tracking and sensing

Jingkun Zhou [1,2,8], Jian Li [1,2,8], Huiling Jia [1,2,8], Kuanming Yao [1,8], Shengxin Jia [1,2], Jiyu Li [1,2], Guangyao Zhao [1], Chun Ki Yiu[1,2], Zhan Gao[1], Dengfeng Li [1], Binbin Zhang[1,2], Ya Huang [1], Qiuna Zhuang[3], Yawen Yang[1], Xingcan Huang [1], Mengge Wu [1], Yiming Liu [1], Yuyu Gao[1], Hu Li[1], Yue Hu[1], Rui Shi[1,4], Meenakshi Mukherji[5], Zijian Zheng [3] & Xinge Yu [1,2,6,7] ✉

The capacity to discern and locate positions in three-dimensional space is crucial for human-machine interfaces and robotic perception. However, current soft electronics can only obtain two-dimensional spatial locations through physical contact. In this study, we report a non-contact position targeting concept enabled by transparent and thin soft electronic skin (E-skin) with three-dimensional sensing capabilities. Inspired by the active electrosensation of mormyroidea fish, this E-skin actively ascertains the 3D positions of targeted objects in a contactless manner and can wirelessly convey the corresponding positions to other devices in real-time. Consequently, this E-skin readily enables interaction with machines, i.e., manipulating virtual objects, controlling robotic arms, and drones in either virtual or actual 3D space. Additionally, it can be integrated with robots to provide them with 3D situational awareness for perceiving their surroundings, avoiding obstacles, or tracking targets.

Skin as one of the largest organ for most biology species, performs a multitude of essential functions such as protection, sensation, temperature regulation, energy storage, nutrient synthesis, and immunity[1–3]. In the natural world, the skin of various fauna possesses numerous fascinating capabilities. Mormyroidea, a superfamily of weakly electric fishes, is capable of employing electric fields to actively detect prey (Fig. 1a). Through their skin, they sense and perceive their surroundings, as well as perform three-dimensional (3D) localization of prey, even if the prey is concealed beneath the mud[4].

In recent years, the rapid development of robotics and Virtual/Augmented Reality (VR/AR) has led to an increased demand for lightweight, portable sensors with the capabilities of precise 3D perception in a non-contact manner for immersive 3D content in various applications[5]. Advances in flexible electronics enable the development of electronic skin (E-skin) in thin and soft formats that maximize conformability with human skin or robotics for conformal integration[6–8]. This significant progress has opened up new possibilities not only for E-skin to realize tactile sensation/feedback[7,9,10] enabled human-machine interface (HMI)[11–18], but also for continuous health monitoring, such as electrocardiogram (ECG)[19,20], sweat[21,22], and other physiological signals[23]. However, existing E-skin faces several limitations: (i). limited gesture recognition capabilities, as devices are based on inertial sensors[24,25], strain sensors[11,12,26,27], ultrasound[28], or electrocardiogram (EMG) signals[29,30] to recognize

[1]Department of Biomedical Engineering, City University of Hong Kong, Hong Kong, China. [2]Hong Kong Centre for Cerebro-Cardiovascular Health Engineering; Hong Kong Science Park, New Territories, Hong Kong, China. [3]Laboratory for Advanced Interfacial Materials and Devices, Department of Applied Biology and Chemical Technology, The Hong Kong Polytechnic University, Hong Kong, China. [4]School of Professional Education and Executive Development, The Hong Kong Polytechnic University, Hong Kong, China. [5]Department of Electrical Engineering, City University of Hong Kong, Hong Kong, China. [6]Shenzhen Research Institute, City University of Hong Kong, Shenzhen, China. [7]Hong Kong Institute for Clean Energy, City University of Hong Kong; Kowloon, Hong Kong, China. [8]These authors contributed equally: Jingkun Zhou, Jian Li, Huiling Jia, Kuanming Yao. ✉e-mail: xingeyu@cityu.edu.hk
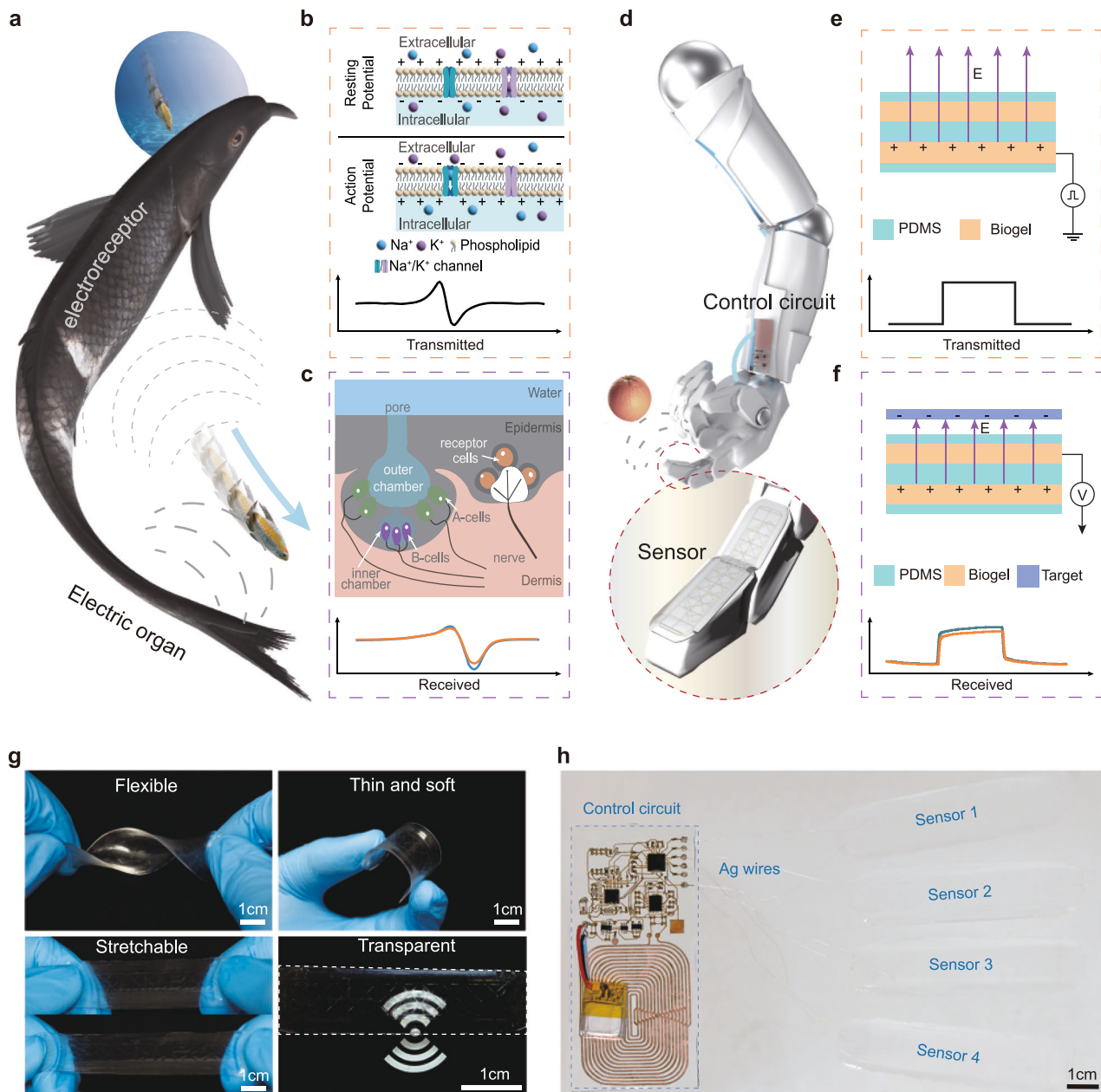
Fig. 1 | Bioinspired transparent E-skin. a Mormyroidea uses its electrical organ and electroreceptor to detect the prey. **b** The working mechanism of the electric organ. **c** Two types of tuberous electroreceptor in Mormyroidea, the Mormyromast (left) and the Knollenorgan (right). **d** Schematic demonstration of a robot using the E-skin to detect the target. **e** The working mechanism of the transmitting electrode. **f** The working mechanism of the receiving electrode. **g** The optical photos of the sensor demonstrate its flexibility, thinness and softness, stretchability, and transparency. **h** The optical photo of a device with discrete sensors.

only a few particular gestures; and (ii). bulky processing systems are typically involved, as the state-of-art technologies are based on imager[31], magnetic field[32], radio frequency[33], or electrostatic theory[34–36].

Mormyroidea skin with active sensing capabilities may be a good inspiration for novel E-skin capable of non-contact and precise 3D spatial positioning with high integration, which is an unexplored topic. The electric organ located in the tail of Mormyroidea controls the migration of potassium ions and sodium ions across cell membranes by switching ion channels, thus discharging the electrical organ and emitting electrical pulses (Fig. 1b)[37]. Specifically, there are two types of tuberous electroreceptors in those fishes, the Mormyromast[38] and the Knollenorgan[39], which detect electric signals of different frequency and intensity (Fig. 1c)[40]. Therefore, they can sense distortions in the

electric field caused by the surrounding objects, and thus targeting the prey[41–43].

In this paper, taking inspiration from the active sensing system of the Mormyroidea, we report a class of materials, devices, electronics, and integration strategy for wireless flexible transparent E-skin with non-contact 3D sensing capability, which consists of Mormyroidea-like sensors and system level soft electronic modules (Fig. 1d). Two patterned biogel electrodes printed on the substrate of Polydimethylsiloxane (PDMS) along with the control circuit are used to imitate electric organs and electroreceptors respectively (Fig. 1e, f). This sensor can actively detect the distance between the target object and the sensor without physical contact. By optimizing its materials and design, this sensor has been rendered with features of flexible, thin, soft, stretchable, and transparent (Fig. 1g). Following that, we

investigated the unique response of flexible sensors such as stretching and bending, which is useful in subsequent analyzes such as noise reduction. By integrating multiple sensor modules and a positioning algorithm into the soft electronic module, the device gains the capability to accurately locate the target in three-dimensional space. On this basis, many non-contact HMI and robotic sensing applications are demonstrated. For different applications, the system supports connecting up to 5 sensors, which can be arranged freely according to actual needs. Figure 1h shows a device with 4 discrete sensors connected via conductive wires (such as silver or copper wires) for maximum flexibility (Fig. 1h). This E-skin can replace traditional rubber-based robot skins, offering protection, increased gripping friction, and high sensitivity to the environment, where the demonstrations associated with the drone performing emergency avoidance and the robotic hands that automatically track the target objects. Its inherent transparency also makes it suitable for complementing the low spatial resolution of IR sensors, enhancing overall performance. Therefore, this work explores the possibility of using soft materials for 3D spatial perception.

Results

Design and working principles of the E-skin

This E-skin comprises two modules, the sensing module and the control circuit module. Figure 2a illustrates the detailed structure of the sensing module with only one sensor. The transmitter (Tx) electrode consisted of patterned biogel (200 µm, ~73.4 kPa[44]) in microchannels of a thin PDMS substrate (300 µm, ~380 kPa[45]). A middle PDMS layer (1000 µm, ~380 kPa) served as the dielectric, with patterned biogel (200 µm, ~73.4 kPa) printed in microchannels on top as the receiver (Rx) electrode. The device was then encapsulated with a thin PDMS layer (100 µm, ~380 kPa). The biogel can withstand a tensile strain over 250% of its original length(Supplementary Fig. 1a), and exhibit great adhesiveness to PDMS, the peel strength is 3.45 mN/mm, which is greater than the widely reported polyacrylamide (PAAm) hydrogel (2.49 mN/mm)[14] (Supplementary Fig. 1b). Due to the presence of sodium ions, the ionic conductivity of the biogel is about 34.3 S/m, affording great electrical performance of the E-skin. Besides, the frequency-impedance curve of the biogel (Supplementary Fig. 1c) shows that it has a good electrical conductivity in the range of 10 kHz to 100 kHz. The biogel's high impedance at low frequencies and low impedance at high frequencies enable it to effectively suppress the influence of low-frequency noise (such as the cable noise), thereby enhancing the sensor's performance. Furthermore, biogel's superior biocompatibility and adjustable properties (conductivity, stimulus responsiveness, and adhesion)[14] make it suitable for this E-skin compared to traditional metal electrodes.

To drive the sensing module and transmit the collected signals wirelessly, we designed a wireless flexible driving circuit as shown in Fig. 2b and Supplementary Fig. 2. This circuit generates a square wave signal with a frequency ~100 kHz to drive the Tx electrode and collects the signal received by the Rx electrodes through high-precision Analog-to-Digital Converters (ADCs). The digital signal can be processed and transmitted to other devices via Bluetooth Low Energy (BLE) by the microcontroller unit (MCU). The circuit also incorporates additional functions, such as wireless charging and capacitive touch buttons, for enhanced convenience. Furthermore, encapsulating the circuit with PDMS renders it impermeable to water, enabling its application in various environments and use cases.

According to the analysis in the supplementary text, in the low-frequency domain (<100 kHz), the electric field dominates the electromagnetic field. When the target object approaches, the distortion in the electric field occurs, inducing electric potential changes on the Rx (Fig. 2c, Supplementary Fig. 3, and Supplementary Movie 1). For quantitative analysis, an equivalent circuit model of this E-skin is shown in Fig. 2d. The Tx and Rx electrodes of the sensor, along with the

PDMS in the middle, form a flat capacitor (C_{Sensor}). A variable capacitance is formed between the target to be measured, such as a human hand, and the Rx electrode (C_{Hand}). Additionally, the capacitance formed by the two electrodes and the system ground C_{RG} and C_{TG}, along with the capacitance between system ground and target with earth ground C_{GND} and C_{HG}, are present in the circuit. The complete derivation of the equation is shown in the "Methods" section, here shows a simplified model. When the drive signal V_{Tx} is applied to the Tx electrode, the received signal on the Rx electrode V_{Rx} can be described as

$$V_{Rx} = V_{Tx} \times \frac{C_{Sensor}}{C_{Sensor} + C_{RG} + C_{Hand}} \tag{1}$$

Equation (1) demonstrates that the received signal is dependent on the capacitance values C_{Sensor} and C_{Hand}, which can be estimated using the parallel plate capacitor formula $C = \varepsilon \cdot \varepsilon_0 \cdot S/d$, where ε is the relative dielectric constant, ε_0 is the vacuum dielectric constant, S is the effective area and d is the distance. A square wave signal with a peak-to-peak value of about 3 V (as shown in Fig. 2e) is fed to the Tx electrode. When a hand approaches the sensor, C_{Hand} increases (S increases and d decreases in the flat capacitor formula), which leads to a decrease of received signal V_{Rx} (Fig. 2e), and vice versa. The response voltage output (V_O) by the circuit is the difference between the voltage with and without a target in the sensing area. The plot of C_{Hand} and V_O from the circuit against distance (Fig. 2f) can be obtained by placing the 'fake finger' (described in the "Methods" section) with a diameter of 8 mm copper foil (to imitate fingertip[46]) at various distances from the sensor (Supplementary Fig. 4). When using the 'fake finger' as a detection target, the detection distance of the sensor can reach up to 10 cm. The signal-to-noise ratio (SNR) of the sensor at different distances from the sensor from 1 cm to 10 cm is shown in Fig. 2g. We also did a sets of reference experiments by adopting copper and liquid metal (LM) as electrode materials for the devices. We found that the output signals from biogel electrodes were comparable to those from copper and LM (Supplementary Fig. 5a). Furthermore, the high impedance at low frequencies of biogel (Supplementary Fig. 1c) can effectively suppress low-frequency noise that may couple into the system. This characteristic of biogel electrodes results in a nearly 10 dB increase in SNR (Supplementary Fig. 5b), enhancing the overall performance of the sensors.

Optimization of the sensor

The shape and size of the Rx electrode determine the C_{Hand} range, and the typical value of C_{Hand} is a few pF. Therefore, improving the sensor's sensitivity is imperative to minimize the value of C_{Sensor}. According to the parallel plate capacitor formula, three parameters can be optimized to reduce C_{Sensor}, the surface area (S) of the capacitor plates, the distance (d) between the plates, and the permittivity (ε) of the dielectric material. (i). To optimize the design parameters of the electrode area (S), multiple sets of experiments with various designs were conducted (Fig. 2h, Supplementary Fig. 6, Supplementary Text, Supplementary Table 1, and 2). As shown in Fig. 2h, the optimized parameters include the hollow area A_{Rx_hatch} and A_{Tx_hatch}, and the width W_{Rx} of the Rx electrode. With the increase of the hollow area on the electrodes by decreasing the wire area of the Tx electrode from 100% to 8.1%, the Rx electrode decreases from 100% to 12.4%, and sensor performance improved by 47%. As the Rx electrode width W_{Rx} decreased (from 28 mm to 8 mm), sensor performance improved by 5%. The device performance was optimal when W_{Rx} matched the target width (8 mm). The V_O - distance curve of sensors with different electrode designs and the optimized design is shown in Fig. 2i (more details can be found in Supplementary Text and Supplementary Fig. 6). The optimized sensor demonstrated a 96% performance improvement over the non-optimized sensor. (ii). We also investigated the
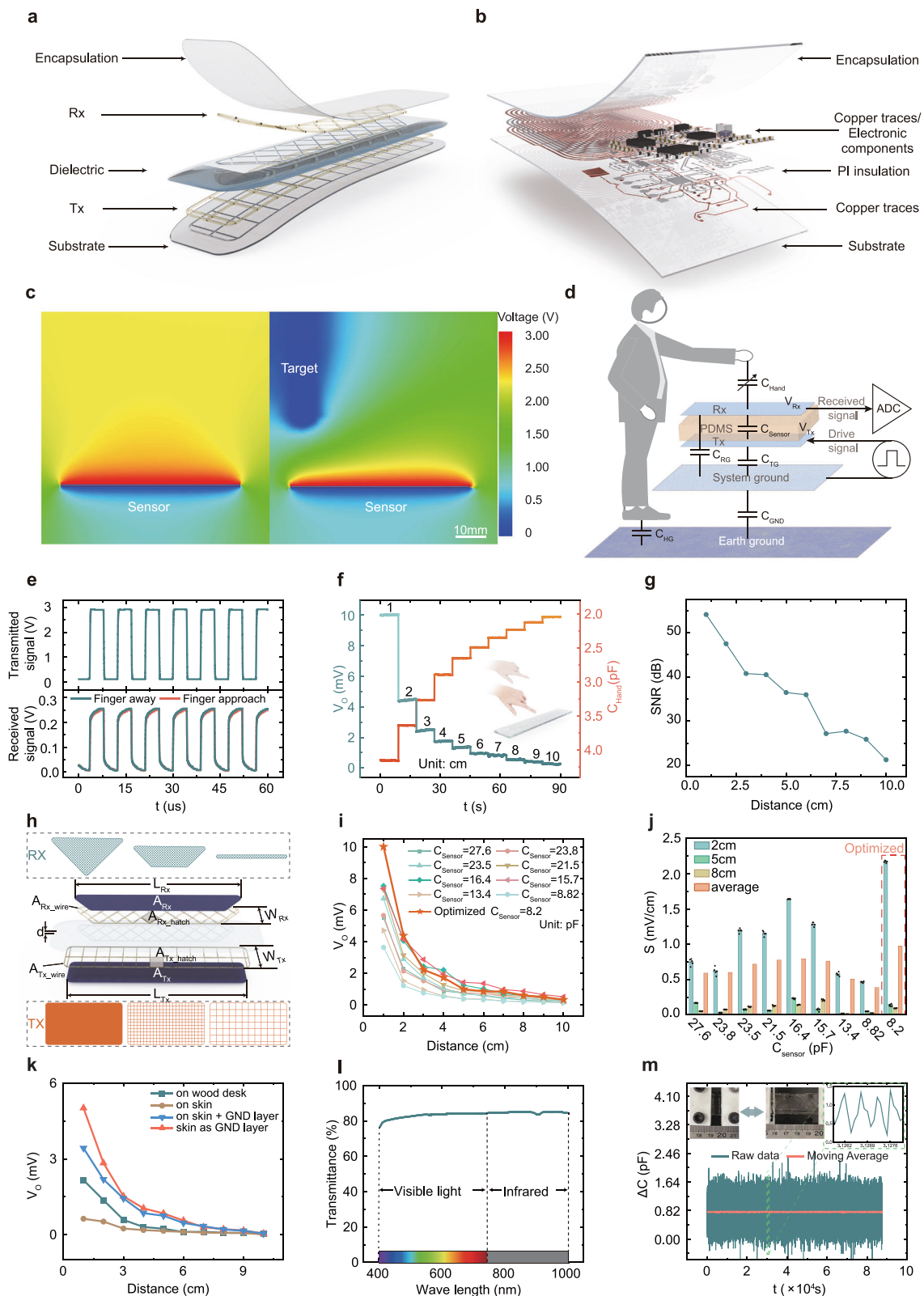
Fig. 2 | The characteristics of the E-skin. a Exploded-view schematic of the sensor module of the E-skin. Rx, receiver; Tx, transmitter. **b** Exploded-view schematic of the control circuit module of the E-skin. ADC, analog-to-digital converters. **c** Simulation of the influence of the target on the electrostatic field. **d** Equivalent circuit model of the E-skin. **e** The signal emitted by the Tx electrode and the received signal on the Rx electrode. **f** C_{Hand} and V_O at different distances between finger and sensor. **g** The SNR of the sensor at different distances from the sensor.

h Schematic diagram of parameters to be optimized. (**i**) Responses and **j** sensitivity of sensors with different electrode designs, and the results of optimized electrodes are highlighted. Bar height, mean; error bars, s.d.; $n = 5$ independent samples. **k** Effect of skin and two shielding schemes on sensor performance. **l** Transmittance of sensor at wavelengths of 400–1000 nm. **m** Capacitance changes during 8800 times folds and unfolds and a 100-point moving average curve to view the overall trend of change. Source data are provided as a Source Data file.

relationship between the thickness of the dielectric d and the sensor's performance (Supplementary Figs. 6e–g). The capacitance value of the C_{Sensor} decreases as d (pure PDMS, dielectric constant of -2.7 at 1 MHz[47]) increases. However, since the capacitance value is inversely related to the thickness d, the decrease in capacitance value gradually slows down with the increase in d (Supplementary Fig. 6g). Hence, a trade-off between the device's thickness and the sensor sensitivity can be found, where the optimized dielectric layer thickness is -0.8 mm to ensure a balanced outcome. (iii). Traditional printed circuit boards (PCB) commonly utilize a dielectric layer (such as FR4) with a dielectric constant of approximately 4.5. By utilizing a thin 0.8 mm PDMS layer as the dielectric material, it is possible to achieve performance comparable to 1.6 mm thick FR4 based sensors. To achieve further reduction in sensor thickness or enhanced sensitivity, we conducted experiments using different dielectric materials with varying dielectric constants (materials preparation is described in the "Method" section). As anticipated from theoretical predictions, we observed that decreasing the dielectric constant from 2.7 (PDMS) to 1.53 (porous PDMS[48]), resulted in an increase in sensor response by 43.3% (Supplementary Fig. 7). This indicates that in certain situations, we can sacrifice transparency or hardness and choose materials with lower dielectric constant to reduce the thickness of the device.

Characteristics of the sensor

In practical applications, numerous factors affect the sensitivity of the sensor. Among these factors, two have significant implications for wearable devices: (i). Capacitances C_{RS} and C_{TS} formed between the skin and the sensor (Supplementary Fig. 8a) are considerably larger than C_{Hand} due to their closer proximity to the skin and greater area overlap with it. These two capacitances are added to the denominator of Eq. (1), which significantly reduces the system's response to C_{Hand} (Supplementary Fig. 8b); (ii). For a non-grounded system (i.e. a lithium-ion battery-powered system), C_{GND} in Fig. 2d should be incorporated into the equation. According to Eq. (2), when C_{GND} approaches 0, the impact of C_{Hand} variation on the output will become insignificant (Supplementary Fig. 8b). To address those issues, a commonly employed method is associated with adding another grounded layer underneath the device to serve as insulation and protect it from environmental changes while increasing the C_{GND} (by increasing system ground area). However, this approach inevitably increases the overall thickness of the device. An alternative method that we propose is to connect the system ground directly to the skin, which can enhance the sensor performance by forming a substantial area for the system ground via the skin. Consequently, C_{RS} and C_{TS} are transferred to C_{RG} and C_{TG} (which have a negligible effect on the output result). Test results in Fig. 2k and Supplementary Fig. 8b demonstrate that this method is more effective than a grounded shield (improved by 46.4%). When the device is attached to the skin, using biogel to connect the ground of the control circuit to human skin can enhance sensor sensitivity (Supplementary Fig. 8c).

Since the dielectric constant of air varies with humidity[49], thereby affects the value of C_{Hand}. So we tested the sensor performance under various air humidity (Supplementary Fig. 9). The biogel used in our sensor is completely encapsulated within a PDMS layer, ensuring it does not come into direct contact with the ambient air. Thus, its parameters remain unaffected by changes in air humidity. The experimental results indicate that the changing trend of the air dielectric constant (Supplementary Fig. 9a) aligns with the varying pattern of sensor performance (Supplementary Fig. 9b). With air humidity varying from 50% to 85% at 20 °C, the change in device output voltage of the device was less than 20%. Furthermore, for certain transparent applications, in pure PDMS as the dielectric material and biogel as the conductive material can achieve light transmittance of over 80% or higher in the 410 nm–1000 nm range (Fig. 2l). This high level of transparency allow the sensor to be used to cover the surface

of existing instruments, such as displays, infrared sensors, etc. (Supplementary Fig. 10). Additionally, as wearable devices, transparent components also facilitate observing negative effects like irritation, allergy, and inflammation, which is crucial for electronic skin applications.

Figure 2j shows the sensitivity of the sensor can reach up to 2.16 mV/cm with a distance of 2 cm. Raising the hand decreases the sensitivity but still can maintain the sensitivity of 0.18 mV/cm at a distance of 10 cm. The SNR can reach up to 54 dB at 1 cm and 21 dB at 10 cm (Fig. 2g). According to the calculation, the distance resolution can reach 5 μm when the target is 1 cm away from the sensor, and at a distance of 10 cm, it could still achieve a resolution of 0.17 mm. To ensure wearer comfort and unrestricted daily activities, the sensor exhibits good stretchability, capable of being stretched up to 172% (Supplementary Fig. 11). Supplementary Fig. 11b shows that when stretched from its original length to 172%, the change in output voltage is less than 30%. Supplementary Figs. 11c–e illustrates the change rate of V_O at different bending radii. Due to the increased distance between the sensor's two ends and the target, the output voltage decreases. However, when bent to a radius of 17.5 mm, the sensor could still retain 54% of its performance. Supplementary Fig. 12 shows the sensitivities at different positions of the sensor. Due to the influence of various factors on the sensor's performance, calibration of the sensor is necessary before use. It's worth mentioning that this sensor has no fatigue effect after long-term wearing under different situations of mechanical strains. This means that the sensor can be stretched and bent repeatedly without experiencing any damage, as demonstrated in Fig. 2m, which shows that there was no significant change of C_{Sensor} after more than 8800 folds and unfolds.

Besides the geometrical parameters of the sensor, the characteristics of the target object also influence the device's performance (Supplementary Fig. 13). Target objects with different sizes, ranging from a diameter of 4 mm to 14 mm have been tested. We found that when the target object increases from 4 mm to 8 mm, the device's response rapidly increases. However, when the target object size exceeds 8 mm, the rate of increase slows down. This is because the sensor's width is 8 mm, so when the target's diameter matches the sensor's width, the device can perform optimally (Supplementary Fig. 13b). With the target size further increases, part of the target's area can't be effectively used to form a capacitance with the sensor, resulting in a slower rate of increase in the device's response (Supplementary Fig. 13a). Secondly, we tested target materials with different resistivities, and we observed that the device's response decreased only 1% when the target's resistivity increased a factor of 10^5 (Supplementary Fig. 13d). The results show that the target materials properties wouldn't affect the sensing performance too much.

When electromagnetic interference (EMI) is present in the environment, such as when a pedestrian passes by, it can also affect the sensor's signal. A test of a person walking from a distance of 1 m to a point 9.5 cm away from the sensor was conducted (the target was placed 5 cm above the sensor, Supplementary Fig. 14a). The result shows that the sensing signal would be interfered when a person entered within 40 cm of the sensor. At a distance of 30 cm from the sensor, the interference reaches 3 %, and at 20 cm, it increases to 18.75 % (Supplementary Fig. 14b). Therefore, additional electromagnetic shielding measures may be necessary in densely populated areas.

Control circuit

Supplementary Fig. 2 illustrates the details of the control circuit. A 3D sensing IC from Microchip is employed to generate the driving signal of Tx and uses built-in high-precision 16-bit ADCs to collect the signals on Rx electrodes. As the capacitance value of C_{Sensor} marginally diminishes (Supplementary Fig. 15a) with an increase in frequency (ranging from 30 k to 100 kHz), the performance of the device also improves with escalating frequencies (Supplementary Fig. 15b). Hence,

the default transmission frequency is set to 100 kHz; however, when the noise power surpasses a certain threshold, the system can automatically switch the transmission frequency to mitigate noise and enhance detection sensitivity. The MCU acquires the filtered sensor data from the 3D sensing IC, computes the 3D coordinates, and then transmits them wirelessly to the smartphone. Upon connecting the lithium-ion battery to the circuit through the capacitive touch switch, the low-dropout regulator (LDO) stabilizes the voltage to a fixed, direct-current voltage for the MCU and 3D sensing IC. Since the supply voltage for ICs such as the MCU is 3.3 V, for the sake of circuit simplicity and power consumption, we directly used this voltage to drive the Tx electrodes. If a longer transmission range is desired, a larger driving voltage of the Tx electrodes can be used (Supplementary Fig. 16). The wireless charging module can receive and convert electromagnetic energy transmitted by the transmitting coil into 5 V voltage to charge the lithium-ion battery. Wireless charging is capable of fully charging an 80 mAh lithium battery in just 30 minutes (Supplementary Figs. 17a, b). In contrast to other systems that rely on mobile phones or computers for complex 3D position calculations on sensor data, our system incorporates a built-in least squares multilateration algorithm (detailed description provided in the Methods) within the MCU. This algorithm can directly calculate the sensor data into real-time three-dimensional coordinates and then transmit them to another device. This device also boasts an intelligent power-saving mode with a meager power consumption of 0.37 mW, enabling it to operate for over 80 hours (Supplementary Fig. 17c). The device operates at full power only when there is a target within the detection area of the sensor. In continuous working mode, the 80 mAh battery can support the circuit for 2 hours (Supplementary Fig. 17d). With an overall power consumption of merely 88 mW, this device surpasses other comparable devices in terms of energy efficiency, which often have power consumption exceeding 200 mW and require external computing resources for calculations. The sampling rate of our device can reach up to 200 samples per second, readily meeting the requirements for standard human-computer interaction. Given that a conventional mouse has a polling rate of only 125 Hz[50], our device can provide sufficient sample responsiveness. Supplementary Fig. 18 portrays the schematic of this circuit.

Contactless human machine interface

A solitary sensor empowers the detection of the distance between the target and the sensor. By amalgamating data from multiple spatially separated sensors (≥ 4), we can ascertain the intersection of multiple spherical surfaces, thereby precisely pinpointing the target's three-dimensional coordination[51] (detailed description is given in the Methods and Supplementary Fig. 19). In contrast to traditional sensors that require a large number of sensor elements to form an array for spatial positioning, our device only needs data from a few sensors to achieve high-precision single-point 3D localization. This significantly reduces the difficulty and power consumption of data collection, transmission, and processing. Due to the inevitable noise contained within the sensor signals, augmenting the number of sensors aids in calculating the target's position with greater accuracy. Figure 3a depicts a user operating the human-machine interaction through the E-skin affixed on the user's arm. As shown in Fig. 3b, the E-skin integrates a control module and a sensing module with 5 sensors (Supplementary Fig. 20), where the whole E-skin exhibits a light weight of 24 g (Supplementary text and Supplementary Table 3 show the comparison with other methods). Upon receiving sensor data, the MCU calculates 3D finger coordinates in real-time, and then sends the data to the computer via BLE. As a result, the GUI displays the finger trajectory and converts it into control signals for the robot. The E-skin is an ideal manipulator for controlling robots, showing the potential to replace the traditional controller, i.e. joysticks, more intuitively. As the finger moves in the sensing area in three axes (left and right, front and

back, up and down), and draws spirals, the real-time coordinates can be displayed on the computer (Supplementary Fig. 21 and Supplementary Movie 2). As a flexible device, elongation will inevitably occur during its use. To investigate the impact of this elongation on spatial positioning, we stretched the e-skin to 170% of its original length while recording changes in spatial positioning (Supplementary Fig. 22). As shown in Supplementary Figs. 19c and d, due to the simultaneous stretching of the five sensors, the changes in signal intensity resulting from the stretching are almost not changed for the predicted X and Y, while there is a slight variation in the Z-axis. The signal variations caused by the distance changes between the sensors and the target are inconsistent across the sensors. To eliminate the impact of these distance-induced signal changes, we synchronized the size of the trajectory drawn by the target with the stretching rate of the sensors (Supplementary Fig. 22a). Consequently, the target position observed at both the unstretched and elongated states (170%) is largely consistent (Supplementary Fig. 22j).

Afterward, we attach the E-skin to a user's arm, allowing the user to intuitively control the motion of robotic arms and drones by simply moving fingers (Fig. 3d and e). Supplementary Fig. 23 and Supplementary Movie 3 show the controlling of a robotic arm by the E-skin-based human-machine interface, where the user uses simple gestures can control the release and grip activities of the robot. As the E-skin is a general method for human-machine interface, drones can be also manipulated by the same E-skin, as shown in Supplementary Fig. 24 and Supplementary Movie 4. The emitting of an electromagnetic field as an active sensing method not only offers the E-skin more sensitive performance in a non-contact way but also gets rid of the influence of handicaps between the E-skin and finger. For instance, placing books, clothes, and other objects between the E-skin and finger does not significantly affect the positioning capabilities (Fig. 3f, Supplementary Fig. 25, and Supplementary Movie 5). Through experiments, we found that inserting 10 sheets of A4 printer paper between the sensor and the target reduces the signal on the sensor by only 0.77%. Inserting 100 sheets of A4 printer paper decreases the sensor's signal by 25.17% (Supplementary Fig. 26). Meanwhile, this E-skin can also act as a Bluetooth mouse or keyboard through HOGP (Human interface device over General agreement on tariffs and trade Profile) technology to operate the cursor, adjust the volume, and so on. Traditional mice can only be operated on a 2D plane, but this technology allows users to operate the mouse in three-dimensional space, making it more suitable for 3D modeling, 3D gaming, and other similar applications. For example, as shown in Fig. 3g, the E-skin serving as a mouse/keyboard allows writing letters in the air, where the motion trajectory calculated by the algorithm can convert the raw signal received by sensors into letters, i.e. "CITYU".

Robotic sensing

Another significant application domain of the E-skin is in robotic sensing, where robots can be equipped with such soft E-skin to exhibit sensory capabilities as Mormyroidea skin does (Fig. 4a). The first demonstration associated with solving collision problems typically happened in drones as the monocular vision on the drone is difficult to judge the distance[52]. As depicted in Figs. 4b, 4 sensors are affixed to the drone, with the control circuit on the bottom of the drone. Each sensor with a weight of only 2 g and the minimized control circuit (not including the wireless charging module) with battery is 2.6 g. The payload capacity of the drone (DJI Tello) is 70 g[53]. The total weight of our device is only 10.6 g, ensuring that the light weight of the E-skin does not affect the flight performance. When the drone nears an obstacle under user control, sensor readings spiked rapidly, signaling the imminent proximity to an obstacle (Fig. 4c). As soon as any sensor's output surpasses a threshold, the computer overrides user control and autonomously accelerates the drone in the opposite direction to avoid collision. Once the obstacle has been circumvented, and the drone has
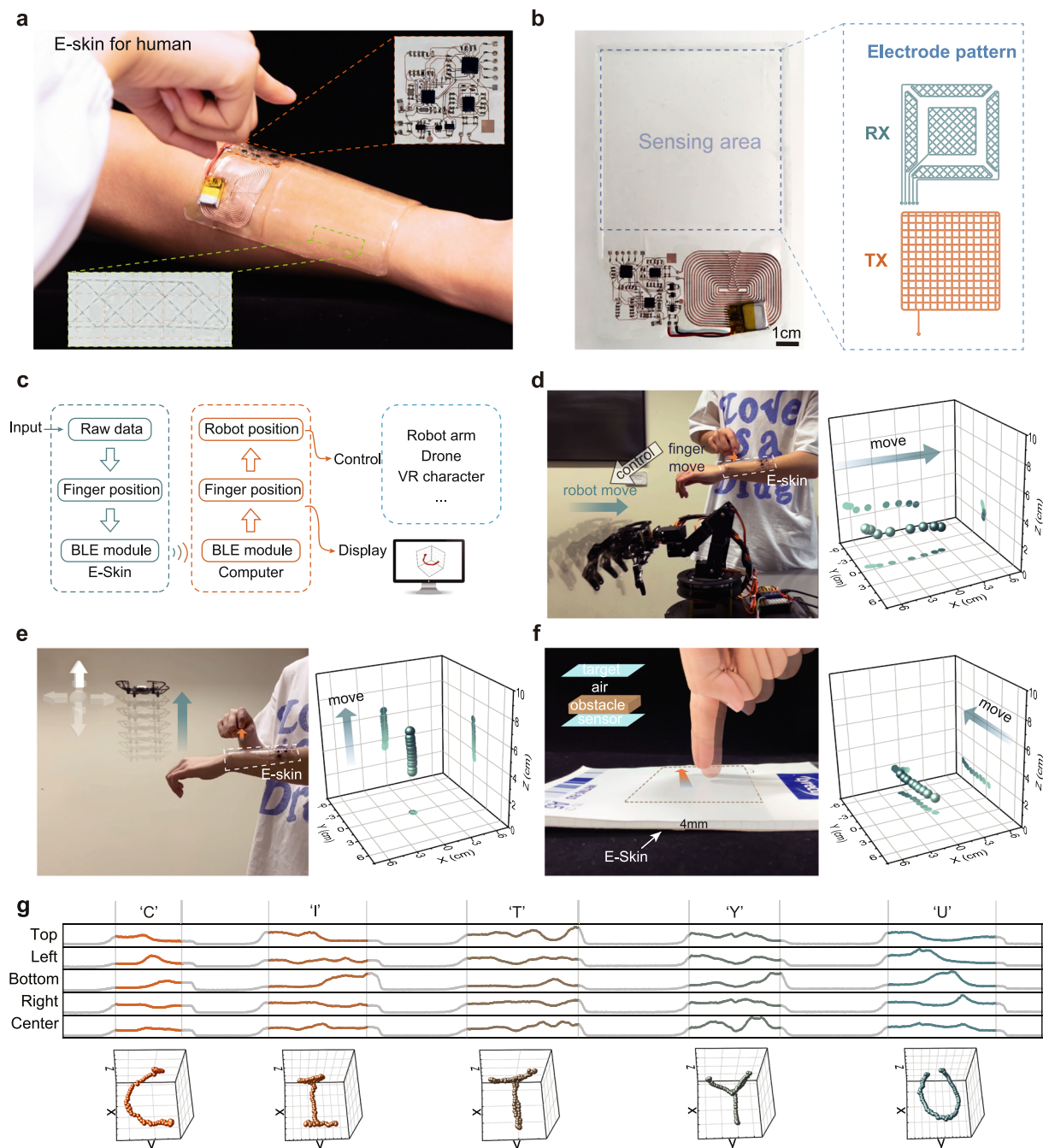
Fig. 3 | Contactless HMI. a Photograph of the E-skin worn on the arm.
b Photograph of the whole E-skin and the electrode patterns on the right. **c** Flow chart of human-machine interaction using E-skin. **d** Photo of using E-skin to control the movement of the robot arm to the right and the data collected by E-skin. **e** Using E-skin to control the drone to fly upwards. **f** E-skin can also work normally even when covered by an obstacle. **g** Write the five letters "CITYU" in the air, the raw data received by the five Rx electrodes, and the image calculated by the algorithm. Source data are provided as a Source Data file.

distanced itself from the obstacle, the sensor's output drops back below the threshold, reinstating user control (Fig. 4c). Figure 4d and Supplementary Movie 6 show the process of the drone flying toward the Universal Serial Bus (USB) cable[49], and accelerating in the opposite direction for braking before collision happening. Real-time raw data was also collected by the four sensors. This demonstration exhibits that this E-skin can supplement the monocular vision limitations of drones, enabling them to detect and avoid obstacles.

In robotic related applications, it is customary to apply rubber-based artificial skin on robots' fingers. This not only protects the robot's fingers from water and dust but also increases friction during object grasping. Our E-skin, while providing these functionalities, additionally endows the robot with the ability to detect target position (Fig. 4e). Once the robot locates the position of the target, it converts the target coordinates collected by the E-skin into world coordinates through its real-time pose and calculates the direction in which it needs to move using the single-neuron PID (proportion integration differentiation) algorithm (Fig. 4f). The detailed single-neuron PID algorithm and inverse kinematics of robotic arm is described in the "Methods" section (Supplementary Fig. 27). In this demo, we set the parameters to keep the target in the palm of the robot hand 2.5 cm away from the E-skin. Figure 4g and Supplementary Movie 7 illustrate
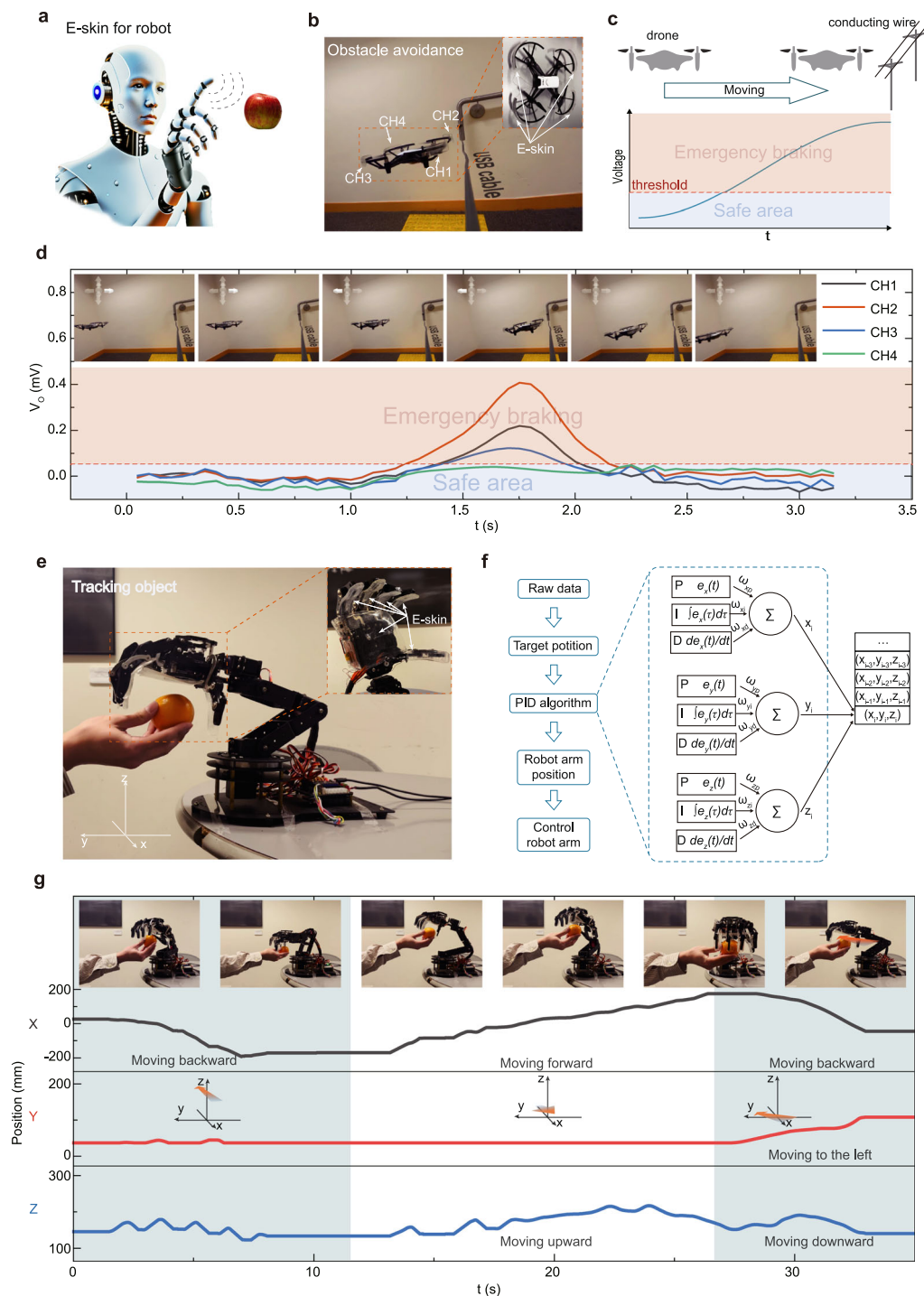
Fig. 4 | Robotic sensing. a Schematic diagram of E-skin for robot perception. **b** Photo of installing E-skin on the drone for obstacle avoidance. **c** Schematic diagram of the principle of drone obstacle avoidance. **d** Photos and real-time data of drone obstacle avoidance. **e** Photo of installing E-skin on the robotic arm for object tracking. **f** Flow chart of a robotic hand for target tracking. **g** Photos of the robotic hand performing target tracking and the 3D coordinates of the robotic hand in space.

the movement of the robotic arm following the orange's movements while always keeping it nearly 2.5 cm away from the palm. This implies that the robot can detect and respond to its surroundings. So, we further explored the practicality of this E-skin on a robotic hand. We conducted an experiment where an operator remotely controlled a robotic hand to grasp an orange, relying solely on a video feed displayed on a computer screen (Figs. 5a, b and Supplementary Movie 8). During two operating sessions, we applied PDMS and E-skin, respectively, to the fingers of the robotic hand. In the E-skin session, after the

robotic hand approached the target, the E-skin detected the nearest object. When the operator pressed the grasp button, the robotic hand automatically fine-tuned its position, aligning the target at the center of the hand before performing the grasping operation. The entire grasping process with the E-skin was completed in nearly half the time compared to the control group (without E-skin). This multi-functional E-skin for future robots enhances their perception capabilities. Infrared (IR) sensors are commonly used in robots for non-contact detection, and due to the transparency of E-skin, it can be placed outside the
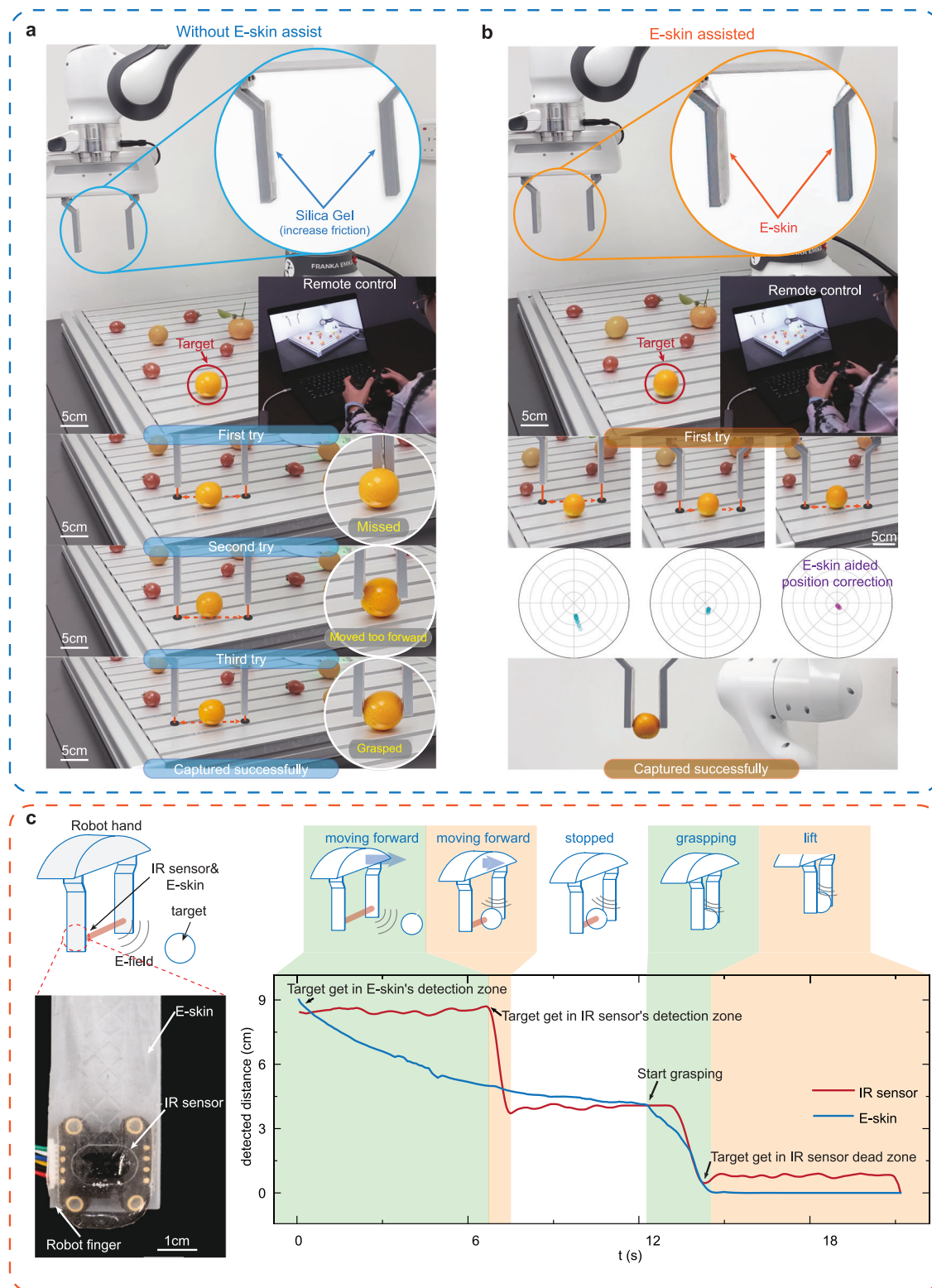
Fig. 5 | Demo of using a robotic arm to grasp a target. An operator remotely controls a robotic arm by watching the streaming video on the screen, **a** without e-skin assistance, the operator relied on video analysis alone to determine the position of the robotic arm, requiring three attempts to successfully grasp the orange; **b** With e-skin assistance, when the operator presses the grasp button, the robotic arm automatically fine-tunes its position to align the object at the center of the two fingers before proceeding with the gripping process. **c** By integrating an IR sensor and E-skin onto the fingers of the robotic hand, the E-skin acts as a flexible interface with enhanced friction and sensing capabilities, compensating for the limitations of the IR sensor. The right side shows the IR sensor and E-skin data during the movement of the robotic hand. It shows that the E-skin can detect objects in the surrounding area and has no dead zones at close range, enabling precise distance detection with the target object. Source data are provided as a Source Data file.

IR sensor to offer additional sensing capabilities and protects the IR sensor while enabling 360-degree target detection (Fig. 5c). This allows targets to enter E-skin's range first as robot hands approach, followed by entering IR sensor's detection range when closer. During grasping, when an object becomes too close for the IR sensor due to its dead zone, E-skin can still detect minute movements within a 1 cm range. By attaching E-skin on the exterior of an IR sensor, both long-distance detection and high precision without any dead zones are combined, enhancing overall performance.

Due to its thin and flexible nature, E-skin can be effectively applied to soft robots. Supplementary Fig. 28a and Supplementary Movie 9 showcases the application of E-skin on a soft robot where, upon approaching fingers, the robot evades; this avoidance repeats when they come even closer. It becomes evident that the presence of E-skin does not significantly affect the motion of the soft robot. As the fingers draw nearer, there is a noticeable fluctuation in the data curve, indicating that despite substantial deformation of the soft robot, the E-skin continues to adhere securely and function stably. We subsequently attached the E-skin to the four fingers of a soft robotic hand and recorded the variations in signal during the grasping of a target object (Supplementary Fig. 28b and Supplementary Movie 10). The data curve reflects the changes in movement by each finger, providing valuable reference for subsequent design and optimization of soft robots.

Finally, considering that this E-skin simulates the active sensing system of Mormyroidea, it should work normally in water (Supplementary Fig. 29a). And because the relative dielectric constant of water (ε_{water} = 81) is much greater than that of air (ε_{air} = 1), the sensor has a significantly higher detection range in water than in air. It can only detect up to 10 cm in air but up to 1 m in water (Supplementary Fig. 29b). However, due to the pressure generated by water fluctuations on the sensor, the noise of the sensor in water is also more pronounced than that in air (Supplementary Fig. 29c). We set a robot fish to swim from one end of a 1 m long tank to the sensor attached to the other end. The sensor can accurately detect the change in distance between the robot fish and the sensor (Supplementary Fig. 29e and Supplementary Movie 11). This E-skin enables divers to operate electronic devices and transmit information to each other through gestures even in dark and murky seabeds. At the same time, it can also help underwater robots explore fish schools in the murky and dark seabed or find marine life hidden under the sand, which is beneficial for studying marine ecology. Further works are also needed to expand the working environments of the sensors, as the current sensor can't detect a target in water with the sensor placed in the air (Supplementary Fig. 30). This is likely due to the low transmittance of electromagnetic waves at the air-water interface[54], which affects the sensor's performance.

Discussion

Our research presents a novel wireless, flexible, and transparent electronic skin (E-skin) inspired by the active sensing system of Mormyroidea, capable of achieving non-contact precise 3D motion detection. Distinguished from existing sensors, our technology employs an active sensing approach by emitting a "radar signal," enabling high spatiotemporal resolution detection of 3D movement and overcoming limitations such as the need for physical contact, high-level integration hurdles with robots, and bulky processing systems. Through the optimization of functional materials and device design, the E-skin exhibits high sensitivity with a distance resolution of 5 μm at 1 cm, stretchability up to 172% without significant performance degradation, and excellent transparency (over 80%) in the visible light range. Comfort and flexibility are ensured by the use of PDMS and biogel, which have Young's moduli similar to skin, making the device soft and comfortable when worn on the body and stretching along with the skin. Improved performance is achieved through the use of biogel as the electrode, providing a response comparable to metal electrodes

but with better SNR and superior stretchability. Additionally, the high transparency of PDMS and biogel allows the device to add 3D sensing functionality to standard screens and integrate with infrared sensors in machine perception applications, thereby improving resolution at close ranges. While more efforts are still needed to expand the E-skin's capabilities, such as realizing multi-finger detection, we believe the E-skin holds broad application prospects in the fields of robotics, VR/AR, and medical applications.

Methods

Ethics statement

All procedures during the testing of human participants are approved by the Human and Artefacts Ethics Sub-Committee, City University of Hong Kong Research Committee. The informed consent of all participants was obtained prior to inclusion in this study.

Fabrication of biogel-based electrodes

The chemicals required for the preparation of biological gels include sodium chloride, sodium citrate, citric acid, glycerol, and gelatin (300-g Bloom). Dissolve 1 g of sodium chloride, 0.1 g of citric acid, 1 g of sodium citrate, and 6 g of glycerol in 8 ml of deionized water, mix on a stirrer for 20 minutes, after which 4 g of gelatin powder should be added and heated in an oven at 75 °C for 4 hours to fully dissolve the gelatin. After cooling, the liquid will transform into a gel due to the physical cross-linking of the gelatin chains and the chemical cross-linking of the citrate ions with the gelatin chains. When using the biogel, just heat it to above 50 °C, and the gel will revert to a liquid state, which will allow it to be extruded from the needle while dispensing, and as the temperature drops to room temperature, the gel will revert to its gel-like state and adhere to the substrate.

The fabrication process of a sensor component is shown in Supplementary Fig. 20. A light-curing 3D printer (Creality Halot Box, Shenzhen Creality 3D Technology Co., Ltd.) with resin (Polyacrylate) is used to manufacture molds with Tx and Rx electrode patterns. Pour the PDMS (Sylgard 184, Dow Corning Corporation, 20:1) into the mold and cure it at 100 °C for 30 minutes to obtain PDMS with electrode patterns. Place the biogel in the barrel and heat the barrel to 50 °C. The dispensing process is then used to inject the biogel into the electrode pattern channels on the PDMS. Finally, PDMS is used to encapsulate the entire device and left to cure at room temperature overnight. The thickness of the bottom layer is 0.3 mm with 0.2 mm microchannels for biogel trace, the thickness of the dielectric layer is 1 mm with 0.2 mm microchannels for biogel trace, the thickness of the biogel trace is 0.2 mm, and the width is 0.2 mm. The overall thickness of the device is ~1.4 mm.

Fabrication of soft circuits

A laser cutter (LPKF ProtoLaser U4, LPKF Laser & Electronics SE) is used to cut out the pattern of two layers of circuit from a PI (30 μm) supported Cu (18 μm) film. The copper wires are then transfer printed to the PDMS substrate, which was prepared in the previous step using a water-soluble tape (Supplementary Fig. 20b). The two layers of the circuit are electrically connected by soldering to the reserved pads with the solder paste. Subsequently, electronic components such as resistors, capacitors, inductors, as well as wireless MCU (CC2640R2F, TI), wireless receiver (BQ51013, TI), 3D gesture recognition chip (MGC3130, Microchip), capacitive touch switch (RH6015C, Rong He), load switch (TPS22919, TI), low dropout regulator (LDO, TPS76933, TI), Bluetooth antenna (2450AT8A100E, Johanson), etc. can be soldered on the manufactured circuit (Supplementary Fig. 2). The application of technologies such as Bluetooth communication, capacitive touch switch, and wireless charging can make this device completely encapsulated with PDMS, without leaving any external wired interfaces, thus the device can achieve good waterproof performance.

Operation of the control circuit

The circuit diagram shown in Supplementary Fig. 2a utilizes the Microchip MGC3130 as the main chip of the sensing module. This chip can generate a 44–115 kHz, 3 V square wave signal on the Tx electrode and has 5 high-precision ADCs built-in, which can simultaneously measure 5 channels of Rx signals. Supplementary Fig. 15 shows the C_{Sensor} value and the received signal strength by Rx when the target is 1 cm away from the sensor at different frequencies. From Supplementary Fig. 15a, it can be seen that as the frequency increases (from 30 kHz to 100 kHz), C_{Sensor} decreases and according to Eq. (1), the output voltage of the sensor will increase. It can be seen from the Supplementary fig. 15b that when the transmission frequency is 100 kHz, the sensor can obtain a larger output signal, that is, higher sensitivity than lower transmission frequency. Therefore, the default transmission frequency of 100 kHz is used, but after the noise exceeds a certain threshold, the system can automatically switch the transmission frequency to reduce noise and increase detection sensitivity. The received signals are filtered by the signal processing unit in the MGC3130 and then sent to the MCU via the I2C (Inter-Integrated Circuit) bus. After receiving the data, the MCU further processes and packages the data and sends it to the smartphone via Bluetooth. Capacitive touch buttons are used as the power switch which can offer more efficient space utilization and flexibility. When the lithium-ion battery is connected to the circuit through the capacitive touch switch, the low-dropout regulator (LDO) regulates the voltage to a fixed, direct-current voltage to MCU and MGC3130. The wireless charging module can receive and convert electromagnetic energy transmitted by the transmitting coil into 5 V voltage to charge the lithium-ion battery. Wireless charging can fully charge an 80 mAh lithium battery in just 30 minutes (Supplementary Figs. 17a, b). The photo of the circuit is shown in the Supplementary Figs. 2b, c.

Deriving system models from the equivalent circuit

As the equivalent circuit shown in Fig. 2d, many capacitors formed between the target (finger), the sensor, and the ground. According to the principle of capacitive voltage division, the received signal on the Rx electrode V_{Rx} can be described as

$$V_{Rx} = V_{Tx} \times \frac{C_{Sensor}}{C_{Sensor} + C_{RG} + \frac{C_{Hand}C_{HG} + C_{Hand}C_{GND} + C_{HG}C_{GND}}{C_{Hand}C_{HG}C_{GND}}} \quad (2)$$

If the system ground is connected directly to the earth ground, then the Eq. (2) can be simplified as

$$V_{Rx} = V_{Tx} \times \frac{C_{Sensor}}{C_{sensor} + C_{RG} + \frac{C_{Hand}C_{HG}}{C_{Hand} + C_{HG}}} \quad (3)$$

By comparing Eq. (2) and Eq. (3), when using a battery as a power source, C_{GND} will be introduced into the equation, which will reduce the variation range of the third term in the denominator as C_{Hand} changes. Therefore reduces the sensitivity of the sensor.

The capacitance values of C_{Sensor} and C_{RG} are typically between 10 pF to 30 pF, and the variation range of C_{Hand} is generally around 2 pF (for fingertip). Therefore, minimizing C_{RG} and C_{Sensor} can effectively improve the sensitivity of the sensor. Due to the $C_{HG} \gg C_{Hand}$, so Eq. (3) can be simplified as Eq. (1).

Fabrication of materials with different dielectric constant

In Supplementary Figs. 7a-d, the porous PDMS material was prepared following a protocol proposed by Juwon's work[48]. To initiate this process, PDMS (Sylgard 184, Dow Corning Corporation, 20:1) and FC-43 (Perfluorotributylamine, Macklin) were mixed in a volumetric ratio of 3:2 using a homogenize at 2000 rpm for 6 minutes. Subsequently, sugar was incorporated into the mixture at varying volume ratios of 4:1, 3:1, 2:1, and 1:1, with each proportion being thoroughly stirred

before proceeding to the next step. The resulting mixture was then poured into a 3D-printed mold and cured at 80 °C for 20 minutes. Subsequent to this, the PDMS was immersed in DI water and placed on a hot plate set at 60 °C for an additional 20 minutes to ensure complete dissolution of sugar within the PDMS matrix. Finally, the porous PDMS was dried on the hot plate at 60 °C until the desired porous structure was obtained.

The materials in Supplementary Figs. 7e and f were prepared through a mixture of PDMS and hollow SiO2 microparticles. Briefly, 10 g of PDMS (base: curing agent, 10:1) was added into the beaker, followed by 10 g of hollow glass microparticles (K25, 3 M) for mixing and stirring at a speed of 800 revolutions per minute (rpm) for 10 min. During the stirring process, 3 ml of Hexane and 10 mg of (3-Aminopropyl) triethoxysilane (APTES, KH55) were also added into the mixture to improve the performance quality of the porous dielectric layer. The final mixture was then poured into the 3D-printed mold. The curing process for the mixture was conducted using two distinct methods: the gradient heating approach (Supplementary Fig. 7e) and the constant high-temperature approach (Supplementary Fig. 7f). In the gradient heating approach, the mixture was cured cure at 40 °C for 10 minutes, followed by a subsequent baking at 80 °C for 20 minutes in an oven. Meanwhile, in the constant high-temperature approach, the mixture was cured at a consistent 80 °C for 30 minutes in an oven. Upon completion of these processes, the resulting cured porous dielectric layer was carefully peeled off from the mold.

Least square for multilateration

Using a single sensor can only determine the distance between the target and that sensor, which allows us to locate the target on a spherical surface. By fusing data from multiple spatially separated sensors (≥ 4), we can determine the intersection of multiple spherical surfaces, thereby pinpointing the target's precise three-dimensional coordinates[51]. Each sensor gives us a sphere of possible target positions; with multiple sensors, the overlap of these spheres yields a single point - the target location. Due to the inevitable noise contained in the sensor signals, the spherical surfaces determined from them may not precisely intersect at a single point. To address this, we use a least-squares algorithm to estimate the most likely target coordinates based on the noisy data. Adding more sensors helps calculate the target's position more accurately by providing additional data to constrain the least-squares estimate. Traditional spatial positioning methods treat both the detecting and measured objects as points, using four reference points to locate the coordinates of the measured object. In order to obtain a stronger signal response and expand the detection range, we use bar-shaped electrodes, so the reference electrodes cannot be treated as points. By modifying the traditional multilateration, we have derived an algorithm for spatial positioning.

First, we can calculate the distance d between the target object and each electrode based on the signal strength received by each Rx electrode. Since the electrodes are bar-shaped, we can draw a cylindrical surface to represent the possible locations where the target may appear, based on the distance d and the position of the electrode. The intersection of the two surfaces formed by the two opposite electrodes will result in a line (Supplementary Fig. 19a). Using two pairs of opposing electrodes, two lines can be obtained, and the intersection of the two lines is the spatial position of the target. This is the algorithm for positioning using four electrodes. In order to improve the accuracy of positioning, a fifth electrode can be introduced (Supplementary Fig. 19b), and in order to prevent the problem of several surfaces not intersecting at one point due to errors, the least squares method is introduced. Suppose the central coordinates of electrodes 1-5 in Supplementary Fig. 19b are $(x_1, y_1, z_1) \ldots (x_5, y_5, z_5)$, the distances from the target are $d_1 \ldots d_5$, and the length and width of electrode 5 is L, then

the following equations can be obtained:

$$
\begin{cases}
(x-x_1)^2 + y - y_1 + (z-z_1)^2 = d_1^2 \\
(x-x_2)^2 + y - y_2 + (z-z_2)^2 = d_2^2 \\
x - x_3 + (y-y_3)^2 + (z-z_3)^2 = d_3^2 \\
x - x_4 + (y-y_4)^2 + (z-z_4)^2 = d_4^2 \\
z - z_5 = d_5 \left(|x-x_5| \le \frac{L}{2}, |y-y_5| \le \frac{L}{2} \right) \\
(x-x_5 \pm \frac{L}{2})^2 + y - y_5 + (z-z_5)^2 = d_5^2 \left(|x-x_5| > \frac{L}{2} \right) \\
x - x_5 + (y-y_5 \pm \frac{L}{2})^2 + (z-z_5)^2 = d_5^2 \left(|y-y_5| > \frac{L}{2} \right)
\end{cases}
\tag{4}
$$

Among them, the fifth electrode is divided into three cases for discussion, corresponding to the target being above the fifth electrode and outside the fifth electrode. We will select the last case to simplify the equation for illustration, and the other cases are similar.

$$
\begin{bmatrix}
2(x_2-x_1) & 0 & 2(z_2-z_1) \\
0 & 2(y_4-y_3) & 2(z_4-z_3) \\
0 & 2(y_5 - \frac{L}{2} - y_4) & 2(z_5-z_4)
\end{bmatrix}
\cdot
\begin{bmatrix} x \\ y \\ z \end{bmatrix}
=
\begin{bmatrix}
d_1^2 - d_2^2 - x_1^2 + x_2^2 + y_1 - y_2 - z_1^2 + z_2^2 \\
d_3^2 - d_4^2 + x_3 - x_4 - y_3^2 + y_4^2 - z_3^2 + z_4^2 \\
d_4^2 - d_5^2 + x_4 - x_5 - y_4^2 + y_5^2 - z_4^2 + z_5^2
\end{bmatrix}
\tag{5}
$$

Equation (5) can be written as:

$$
\mathbf{AX} = \mathbf{B}
\tag{6}
$$

Set the error vector as $\boldsymbol{\varepsilon} = \mathbf{AX} - \mathbf{B}$, then the square of the error is

$$
\mathbf{E} = |\boldsymbol{\varepsilon}|^2 = \boldsymbol{\varepsilon}^T \boldsymbol{\varepsilon} = (\mathbf{AX} - \mathbf{B})^T (\mathbf{AX} - \mathbf{B})
\tag{7}
$$

To minimize the error, the derivative of Eq. (7) is

$$
\frac{d\mathbf{E(X)}}{d\mathbf{X}} = 2\mathbf{A}^T \mathbf{AX} - 2\mathbf{A}^T \mathbf{B} = 0
\tag{8}
$$

Solving the Eq.(8),

$$
\mathbf{X} = (\mathbf{A}^T \mathbf{A})^{-1} (\mathbf{A}^T \mathbf{B})
\tag{9}
$$

The spatial position of the target can be obtained by simultaneously calculating the different cases of the fifth electrode and selecting the appropriate z coordinate according to the calculated x, y coordinates.

Single-neuron PID control

The traditional PID algorithm has a problem in that the parameters are set at the time of designing the algorithm, while the learning ability of neural networks can make up for the shortcomings of the traditional PID algorithm very well[55]. If we denote $x_1 = e(t), x_2 = \int e(\tau)d\tau, x_3 = \frac{de(t)}{dt}$, where e(t) is the error at time t, then the traditional PID algorithm we can write as

$$
\Delta u(t) = K \left(\sum_{i=1}^{3} \omega_i'(t) x_i(t) \right)
$$

Where $u(t)$ is the control signal at time t, $\omega_i'(t) = \omega_i(t) / \sum_{i=1}^{3} |\omega_i(t)|$, ω_i are the coefficients of the proportional, integral, and differential, K is the scaling factor.

Updating coefficients ω_i by using supervised Hebb rules

$$
\Delta \omega_i(t) = \eta_i e(t) u(t) x_i(t)
$$

Where η_i is the learning speed.

By adding a learning algorithm, the PID algorithm can automatically adjust the parameters during operation and has stronger anti-interference capability.

Characterization

Voltage is tested using an oscilloscope (Rigol DS1054Z), with a bandwidth of 50 MHz. The capacitance change is measured using an LCR meter (TH2832, Tonghui). The device transmittance is measured using a UV/VIS Spectrophotometer. The tensile modulus and peel strength of the bio-gel are measured using the Instron tensile tester 5942. Impedance and electrical resistivity of biogel were measured using CHI660E. The dielectric constant of the dielectric material was obtained through testing using an Agilent 4294 A Precision Impedance Analyzer at a frequency of 100 kHz.

In order to measure the sensitivity of the device, we used a 3D printer to print a test bracket (Supplementary Fig. 4) with resin to minimize the influence of factors like shaking, pose, etc. of the finger. The height of the bracket can be adjusted by replacing different-length arms. We placed the device on a wooden desk, keeping the body and other conductive objects more than 50 cm away from the device to reduce the influence. An 8 mm diameter copper foil was attached to the head of the test bracket as the target to be tested, and a fine copper wire was connected between the copper foil and the human body. We call the artificial test bracket the 'fake finger'. Put the head of the 'fake finger' into the sensor's sensing area to test. By adjusting the distance between the head of the 'fake finger' and the sensor from 1-10 cm, the relationship between the sensor response and the distance can be obtained.

Inverse kinematics of robot arm

From Supplementary Fig. 27, (x, y, α) is the final posture of the robot arm, x, y are the coordinates of the end of robot arm on the XOY plane, α is the angle between the end of the robot arm and the horizontal plane. We can get the system of equations:

$$
\begin{cases}
x = l_0 \cos\theta_1 + l_1 \cos(\theta_1 + \theta_2) + l_2 \cos(\theta_1 + \theta_2 + \theta_3) \\
y = l_0 \sin\theta_1 + l_1 \cos(\theta_1 + \theta_2) + l_2 \sin(\theta_1 + \theta_2 + \theta_3) \\
\alpha = \theta_1 + \theta_2 + \theta_3
\end{cases}
$$

Solve the system of equations above, we can get

$$
\theta_1 = \operatorname{asin}\left(\frac{-b \pm \sqrt{b^2 - 4ac}}{2a} \right)
$$

Where

$$
k = \frac{l_0^2 - l_1^2 - m^2 - n^2}{2l_1}
$$
$$
a = m^2 + n^2
$$
$$
b = -2nk
$$
$$
c = k^2 - m^2
$$

Similarly, θ_2 can be solved, and $\theta_3 = \alpha - \theta_1 - \theta_2$.

Robots control

The robotic arm and robotic hand in Figs. 3 and 4 were purchased from Zhongling Technology. They use an Arduino Uno as the control board to control the movement of the robotic arm and robotic hand by receiving commands transmitted from the computer through a universal asynchronous receiver/transmitter (UART). On the computer side, we use the self-developed Python program to call the computer Bluetooth module to receive the position information from the E-skin, perform PID computing, inverse kinematics analysis, and send commands to the Arduino Uno. The robotic arm in Fig. 5 is a commercially procured Franka Emika Panda. It is operated through the Franka Control Interface (FCI) in conjunction with self-developed Python code.

The drone is DJI Tello, which can be controlled by a computer through a Python code. A self-developed Python program is used to collect the data from the E-skin and control the flight of the drone.

Electromagnetism simulation

The finite element analysis (FEA) was conducted with commercial electromagnetic analysis software MAXWELL, where a triangle element was used to model the geometry. An adaptive meshing convergence condition was adopted, and a rectangle radiation boundary, with a boundary size of 110 mm × 200 mm, was used to ensure calculation accuracy. The conductive gel was modeled by a conductor with a conductivity of 34 S/m. The dielectric layer of PDMS was modeled by dielectric material with a dielectric constant of 2.7. A DC voltage with an amplitude of 3 V was applied to the lower electrode. This simulation result shows the change of electric potential on the Rx electrode when the electric potential on the Tx electrode is 3 V. The electric potential at infinity and the target surface is 0 V.

Reporting summary

Further information on research design is available in the Nature Portfolio Reporting Summary linked to this article.

Data availability

All data supporting the results of this study are available within the paper and its Supplementary Information. Source data are provided with this paper.

Code availability

The code used in this work is available at the following link: https://doi.org/10.5281/zenodo.13993132.

References

1. Gratton, R., Del Vecchio, C., Zupin, L. & Crovella, S. Unraveling the role of sex hormones on keratinocyte functions in human inflammatory skin diseases. *Int J. Mol. Sci.* **23**, 3132 (2022).
2. Kiatsurayanon, C., Ogawa, H. & Niyonsaba, F. The role of host defense peptide human β-defensins in the maintenance of skin barriers. *Curr. Pharm. Des.* **24**, 1092–1099 (2018).
3. Proksch, E., Brandner, J. M. & Jensen, J.-M. The skin: an indispensable barrier. *Exp. Dermatol* **17**, 1063–1072 (2008).
4. Nelson, M. E. & MacIver, M. A. Sensory acquisition in active sensing systems. *J. Comp. Physiol. A* **192**, 573–586 (2006).
5. Mitra, S. & Acharya, T. Gesture recognition: a survey. *IEEE Trans. Syst., Man, Cybern., Part C. (Appl. Rev.)* **37**, 311–324 (2007).
6. Benight, S. J., Wang, C., Tok, J. B. H. & Bao, Z. Stretchable and self-healing polymers and devices for electronic skin. *Prog. Polym. Sci.* **38**, 1961–1977 (2013).
7. Yu, X. et al. Skin-integrated wireless haptic interfaces for virtual and augmented reality. *Nature* **575**, 473–479 (2019).
8. Li, D., Yao, K., Gao, Z., Liu, Y. & Yu, X. *Recent Prog. Ski. -Integr. Electron. Intell. Sens. gxjzz* **2**, 39 (2021).
9. Li, D. et al. Touch IoT enabled by wireless self-sensing and haptic-reproducing electronic skin. *Sci. Adv.* **8**, eade2450 (2022).
10. Yao, K. et al. Encoding of tactile information in hand via skin-integrated wireless haptic interface. *Nat. Mach. Intell.* **4**, 893–903 (2022).
11. Liu, Y. et al. Electronic skin as wireless human-machine interfaces for robotic VR. *Sci. Adv.* **8**, eabl6700 (2022).
12. Kim, K. K. et al. A substrate-less nanomesh receptor with meta-learning for rapid hand task recognition. *Nat. Electron* **6**, 64–75 (2023).
13. Kim, K. K. et al. Transparent wearable three-dimensional touch by self-generated multiscale structure. *Nat. Commun.* **10**, 2582 (2019).
14. Kim, C.-C., Lee, H.-H., Oh, K. H. & Sun, J.-Y. Highly stretchable, transparent ionic touch panel. *Science* **353**, 682–687 (2016).
15. Shim, H. et al. Stretchable elastic synaptic transistors for neurologically integrated soft engineering systems. *Sci. Adv.* **5**, eaax4961 (2019).
16. Park, J. et al. Stretchable ionic composites for strain-insensitive dual-mode pressure and proximity sensors. *Chem. Eng. J.* **480**, 148172 (2024).
17. Huang, L. et al. Research progress of multifunctional flexible proximity sensors. *Sens. Actuators A: Phys.* **360**, 114500 (2023).
18. Park, J. et al. Soft sensors and actuators for wearable human–machine interfaces. *Chem. Rev.* **124**, 1464–1534 (2024).
19. Yiu, C. et al. Soft, stretchable, wireless intelligent three-lead electrocardiograph monitors with feedback functions for warning of potential heart attack. *SmartMat.* **3**, 668–684 (2022).
20. Chung, H. U. et al. Binodal, wireless epidermal electronic systems with in-sensor analytics for neonatal intensive care. *Science* **363**, eaau0780 (2019).
21. Huang, X. et al. Epidermal self-powered sweat sensors for glucose and lactate monitoring. *Bio-Des. Manuf.* **5**, 201–209 (2022).
22. Bariya, M., Nyein, H. Y. Y. & Javey, A. Wearable sweat sensors. *Nat. Electron* **1**, 160–171 (2018).
23. Lee, K. et al. Mechano-acoustic sensing of physiological processes and body motions via a soft wireless device placed at the suprasternal notch. *Nat. Biomed. Eng.* **4**, 148–158 (2020).
24. Galka, J., Mąsior, M., Zaborski, M. & Barczewska, K. Inertial motion sensing glove for sign language gesture acquisition and recognition. *IEEE Sens. J.* **16**, 6310–6316 (2016).
25. Fang, B., Sun, F., Liu, H. & Liu, C. 3D human gesture capturing and recognition by the IMMU-based data glove. *Neurocomputing* **277**, 198–207 (2018).
26. Wu, H. et al. Fabric-based self-powered noncontact smart gloves for gesture recognition. *J. Mater. Chem. A* **6**, 20277–20288 (2018).
27. Wen, F. et al. Machine learning glove using self-powered conductive superhydrophobic triboelectric textile for gesture recognition in VR/AR applications. *Adv. Sci.* **7**, 2000261 (2020).
28. Yan, J., Yang, X., Sun, X., Chen, Z. & Liu, H. A lightweight ultrasound probe for wearable human–machine interfaces. *IEEE Sens J.* **19**, 5895–5903 (2019).
29. Moin, A. et al. A wearable biosensing system with in-sensor adaptive machine learning for hand gesture recognition. *Nat. Electron* **4**, 54–63 (2021).
30. Kwon, Y.-T. et al. All-printed nanomembrane wireless bioelectronics using a biocompatible solderable graphene for multimodal human-machine interfaces. *Nat. Commun.* **11**, 3450 (2020).
31. Kamijo, T. et al. A touchless user interface based on a near-infrared-sensitive transparent optical imager. *Nat. Electron* 1–11, https://doi.org/10.1038/s41928-023-00970-8 (2023).
32. Cañón Bermúdez, G. S. et al. Magnetosensitive e-skins with directional perception for augmented reality. *Sci. Adv.* **4**, eaao2623 (2018).
33. Ahmed, S., Kallu, K. D., Ahmed, S. & Cho, S. H. Hand Gestures Recognition Using Radar Sensors for Human-Computer-Interaction: A Review. *Remote Sens-Basel* **13**, 527 (2021).
34. Guo, Z. H. et al. Bioinspired soft electroreceptors for artificial precontact somatosensation. *Sci. Adv.* **8**, eabo5201 (2022).
35. Zhu, S. et al. An artificial remote tactile device with 3D depth-of-field sensation. *Sci. Adv.* **8**, eabo5314 (2022).
36. Liu, W. et al. Touchless interactive teaching of soft robots through flexible bimodal sensory interfaces. *Nat. Commun.* **13**, 5030 (2022).
37. Lissmann, H. W. Continuous electrical signals from the tail of a fish, Gymnarchus niloticus Cuv. *Nature* **167**, 201–202 (1951).
38. Bell, C. C., Zakon, H. & Finger, T. E. Mormyromast electroreceptor organs and their afferent fibers in mormyrid fish: I. Morphology. *J. Comp. Neurol.* **286**, 391–407 (1989).
39. Derbin, C. & Szabo, T. Ultrastructure of an electroreceptor (knollenorgan) in the mormyrid fish Gnathonemus petersii. I. *J. Ultrastruct. Res.* **22**, 469–484 (1968).

40. Bennett, M. V. L. Electroreceptors in mormyrids. in *Cold Spring Harbor Symposia on Quantitative Biology*. **30**, 245–262 (Citeseer, 1965).

41. Smith, J. R. *Electric Field Imaging*. (Massachusetts Institute of Technology, 1999).

42. Gottwald, M., Singh, N., Haubrich, A. N., Regett, S. & von der Emde, G. Electric-color sensing in weakly electric fish suggests color perception as a sensory concept beyond vision. *Curr. Biol.* **28**, 3648–3653.e2 (2018).

43. Skeels, S. E. *Sensory-motor Integration In Gnathonemus Petersii*. (University of Oxford, 2022).

44. Wang, C. et al. On-skin paintable biogel for long-term high-fidelity electroencephalogram recording. *Sci. Adv.* **8**, eabo1396 (2022).

45. Song, E. et al. Miniaturized electromechanical devices for the characterization of the biomechanics of deep tissue. *Nat. Biomed. Eng.* **5**, 759–771 (2021).

46. Cleary, F. & Microchip Technology Inc. Capacitive Touch Sensor Design Guide (AN2934). Microchip https://www.microchip.com/en-us/application-notes/an2934 (2020).

47. Mark, J. E. Polymer Data Handbook, 2nd ed. *J. Am. Chem. Soc.* **131**, 16330–16330 (2019).

48. Hwang, J., Kim, Y., Yang, H. & Oh, J. H. Fabrication of hierarchically porous structured PDMS composites and their application as a flexible capacitive pressure sensor. *Compos. Part B: Eng.* **211**, 108607 (2021).

49. Zhou, B., Zhang, K., Li, Y., Yang, L. & Ni, J. Study on measurement error of power frequency electric field intensity caused by change of air dielectric constant with humidity. *IOP Conf. Ser.: Earth Environ. Sci.* **772**, 012022 (2021).

50. Jorgensen, Z. & Yu, T. *On Mouse Dynamics As A Behavioral Biometric For Authentication*. in *Proceedings of the 6th ACM Symposium on Information, Computer and Communications Security* 476–482 (Association for Computing Machinery, New York, NY, USA, 2011).

51. Luo, Q. et al. An improved trilateration positioning algorithm with anchor node combination and k-means clustering. *Sens. -Basel* **22**, 6085 (2022).

52. Wang, L. et al. Applications and prospects of agricultural unmanned aerial vehicle obstacle avoidance technology in China. *Sens. -Basel* **19**, 642 (2019).

53. Malczan, A. N. How much weight can a drone carry? (lb & kg). Droneblog https://www.droneblog.com/drone-payload/ (2021).

54. Jiang, S. & Georgakopoulos, S. Electromagnetic wave propagation into fresh water. *J. Electromagn. Anal. Appl.* **3**, 261–266 (2011).

55. Sheng, Q., Xianyi, Z., Changhong, W., Gao, X. Z. & Zilong, L. *Design And Implementation Of An Adaptive Pid Controller Using Single Neuron Learning Algorithm*. in *Proceedings of the 4th World Congress on Intelligent Control and Automation (Cat. No.02EX527)* 2279–2283 (IEEE, Shanghai, China, 2002).

Acknowledgements

Author contributions

J.Z., J.L., H.J., and K.Y. contributed equally to this work. X.Y. and J.Z. conceived the idea and designed the projects. J.Z., J.L., H.J., K.Y., S.J., Jiyu L., and G.Z. fabricated the device and performed the other experiments. J.Z., J.L., and K.Y. designed the E-skin. H.J., C.K.Y., and Y.Y. designed the algorithm. J.L., B.Z. conducted the mechanical modeling. S.J. and J.Z. conducted the robot experiments. Jiyu L., Z.G., D.L., Y.H. and Q.Z. fabricated dielectric materials. J.Z. and X.Y. wrote the manuscript. X.H., M.W., Y.L., Y.G., H.L., Y.H., R.S., M.M. and Z.Z. contributed to discussing the data and commenting on the manuscript.

Competing interests

The authors declare no conflict of interest.

Additional information

Supplementary information The online version contains supplementary material available at https://doi.org/10.1038/s41467-024-54249-3.

Correspondence and requests for materials should be addressed to Xinge Yu.

Peer review information *Nature Communications* thanks the anonymous reviewers for their contribution to the peer review of this work. A peer review file is available.

Reprints and permissions information is available at http://www.nature.com/reprints

Publisher's note Springer Nature remains neutral with regard to jurisdictional claims in published maps and institutional affiliations.